

Optimization of cross flow heat exchangers for thermoelectric waste heat recovery

Douglas T. Crane, Gregory S. Jackson *

Department of Mechanical Engineering, University of Maryland, College Park, MD 20742, USA

Received 18 January 2003; received in revised form 28 August 2003; accepted 1 September 2003

Abstract

Thermoelectric waste heat recovery is investigated for current thermoelectric materials with advanced heat exchangers. Numerical heat exchanger models integrated with models for Bi_2Te_3 thermoelectric modules are validated against experimental data from previous cross flow heat exchanger studies as well as experiments using thermoelectrics between counterflow hot water and cooling air flow channels. The models are used in optimization studies of thermoelectric waste heat recovery with air cooling in a cross flow heat exchanger. Power losses from an air fan and a fluid pump result in an optimal configuration at intermediate cooling air and hot fluid flows. Results show that heat exchangers with Bi_2Te_3 thermoelectrics can achieve net power densities over 40 W/l.

© 2003 Elsevier Ltd. All rights reserved.

Keywords: Thermoelectric; Waste heat recovery; Power generation; Optimization; Heat exchanger

1. Introduction

Historically, power generation from waste heat streams using thermoelectric (TE) materials has been overlooked due to low thermal efficiencies (typically $\eta_{\text{th}} < 4\%$). The two limiting factors in TE waste heat recovery are TE conversion efficiency (η_{TE} = electric work produced/heat flux through TE material) and, to a lesser extent, effective heat exchanger design. η_{th} is related to η_{TE} by the following equation:

$$\eta_{\text{th}} = \varepsilon \eta_{\text{TE}} \quad (1)$$

* Corresponding author. Tel.: +1-301-405-2368; fax: +1-301-314-9477.

E-mail address: gsjackso@eng.umd.edu (G.S. Jackson).

Nomenclature

| | |
|---------------------------------|---|
| A_{ht} | total external heat transfer area (m ²) |
| A_0 | minimum free flow area (m ²) |
| A_{core} | frontal area of heat exchanger (m ²) |
| C_p | specific heat capacity at constant pressure (J/kg K) |
| d_{maj}, d_{min} | major and minor dimensions of hot fluid tubes (m) |
| d_{tube} | hydraulic diameter of hot fluid channel (m) |
| f | Fanning friction factor |
| h | heat transfer coefficient (W/m ² K) |
| I_{TE} | current (A) |
| j | Colburn factor |
| K_{TE} | thermal conductance of thermoelectric couples (W/K) |
| l_{fin} | height of fins in air flow passage (m) |
| l_{louv} | height of louvers (m) |
| l_{TE} | height of TE couples (m) |
| \dot{m} | mass flowrates of air and hot fluid (kg/s) |
| n_{TE} | number of couples per unit surface area of hot fluid tube |
| Nu | Nusselt number |
| p_{fin} | pitch of fins (m) |
| p_{louv} | pitch of louvers on fins (m) |
| p_{tube} | spacing between tubes (m) |
| P | pressure in flows (Pa) |
| Pr | Prandtl number |
| \dot{Q}_{TE} | total rate of heat dissipated through thermoelectrics (W) |
| $\dot{q}_{sc}, \dot{q}_{sh}$ | heat flux per unit area of tube wall (W/m ²) |
| R | electrical resistance (Ω) |
| Re | Reynolds number |
| T | temperatures of air flow, hot fluid flow, and thermoelectrics (K) |
| T_{sc}, T_{sh} | cold side and hot side temperatures of TE legs (K) |
| t_{fin} | fin thickness (cm) |
| \dot{V} | volume flow rate of air and hot fluid (m ³ /s) |
| V_{core} | heat transfer volume of heat exchanger (m ³) |
| $\dot{W}_{pump}, \dot{W}_{fan}$ | power demanded by fluid pump or cooling air fan (W) |
| \dot{W}_{TE} | total power generated by TEs (W) |
| \dot{w}_{TE} | power generated per unit area of hot fluid tube (W/m ²) |
| w_{TE} | width of individual TE leg (cm) |
| x | axial distance along hot fluid tube flow axis (m) |
| Z | figure of merit of thermoelectric (K ⁻¹) |
| $\$_{HE}$ | heat exchanger costs |
| $\$_{TE}$ | thermoelectric costs |

Greek symbols

| | |
|-----------------|--|
| α | Seebeck coefficient (V/K) |
| ε | heat transfer effectiveness |
| ε_s | surface roughness |
| λ | thermal conductivity of fluids or TE material (W/m K) |
| η_{TE} | conversion efficiency of TE modules |
| η_{th} | overall efficiency of waste heat conversion to electricity |
| ρ | density of flows (kg/m ³) or electrical resistivity of TE material (Ω m) |
| ρ_c | contact electrical resistivity (Ω m ²) |
| σ | ratio of minimum free flow area to frontal area |
| θ | louver angle (°) |
| μ | dynamic viscosity (kg/m s) |

Subscripts

| | |
|----|----------------|
| a | air flow |
| f | hot fluid flow |
| TE | TE materials |

where ε is the fraction of waste heat passed through the TE couples. η_{TE} of a thermoelectric power generator depends on the material's non-dimensional figure of merit, $ZT = (\alpha_{TE}^2 T / \rho_{TE} \lambda_{TE})$ where the average temperature of the TE couples is $T = (T_{sh} + T_{sc})/2$, and the material properties α , ρ and λ are averaged between the specific properties of the n- and p-legs of the TE as discussed in previous references [1]. Analysis for η_{TE} in an optimized configuration [1] reveals how η_{TE} improves by increasing T_{sh} and decreasing T_{sc} , as indicated in Eq. (2).

$$\eta_{TE} = \frac{m' \left(1 - \frac{T_{sc}}{T_{sh}}\right)}{\frac{(1+m')^2}{ZT_{sh}} + (1+m') - \frac{1}{2} \left(1 - \frac{T_{sc}}{T_{sh}}\right)} \quad (2)$$

where m' is the ratio of the load resistance to the total internal resistance of the TE couples. η_{TE} can be readily shown to be a monotonically increasing function of ZT_{sh} . For maximum efficiency, $m' = (1 + Z(T_{sh} + T_{sc})/2)^{1/2}$, and for maximum power output, $m' = 1$ [1,2]. The thermal efficiency of the waste heat recovery process can then be evaluated in combination with heat transfer analysis to determine ε .

Recent advances in materials and materials processing as summarized in recent reviews [3–5] have led to higher ZT values and, thus, higher theoretical η_{TE} . For large $T_{sh} - T_{sc}$ (>500 K), TE modules combining various materials in long segmented couples have exhibited η_{TE} near 15% or more for $T_{sh} \geq 850$ K [6,7]. These multi-component TE couples may have applications in designs where relatively high temperature heat sources are available and where TE size does not greatly impact heat exchanger effectiveness. For applications where T_{sc} is well below room temperature, ZT up to 2.4 [8] have been discussed for T_{sh} near room temperature. Very high ZT s have also been discussed for proposed quantum well TE devices [9] such that η_{TE} may approach 20% for some applications.

For higher temperature applications, new TE materials, such as Zn_4Sb_3 based semiconductors [5] and skutterudites [3,5,6,10], offer improved η_{TE} , much higher than the 5% of Bi_2Te_3 , but to achieve such performance with these new materials T_{sh} must be >600 K. For waste heat recovery applications, such high temperatures require direct heat transfer from gas phase exhaust streams or the use of expensive high temperature liquids, such as liquid metals. In general, direct heat transfer from gas phase exhaust flows will result in either a low ε or a large power penalty in terms of pressure drop across the heat exchanger. To operate effectively for waste heat recovery applications where inexpensive fluids, such as water or water/glycol mixtures, are used to extract the heat from exhaust flows (as in automotive radiators or most cooling tower applications), TE materials must operate effectively at $350 \text{ K} < T_{\text{sh}} < 400 \text{ K}$. With presently available materials, Bi_2Te_3 based semiconductors offer the best performance for this temperature range with ZT approaching 1.1 [5]. For $T_{\text{sh}} \approx 120^\circ\text{C}$ and $T_{\text{sc}} \approx 20^\circ\text{C}$, this ZT gives η_{TE} up to 5% from Eq. (2). The relatively affordable Bi_2Te_3 TEs are still one of the more attractive options for waste heat recovery and are the focus of the current study.

Previous experiments have investigated waste heat recovery using Bi_2Te_3 TEs and have shown overall waste heat recovery efficiencies (η_{th}) $< 4\%$ [11,12]. Examination of the results reveals that the heat exchanger design on both the hot and cold sides of the TEs significantly impacts η_{th} . The current study addresses issues related to optimizing TE waste heat recovery by integrating efficient cross flow heat exchangers with thermoelectric modules for conversion of waste heat to electricity. Numerical heat exchanger models are integrated with models for Bi_2Te_3 TE modules, which are positioned between the hot and cold flow streams as shown in the schematic of a heat exchanger sub-section in Fig. 1. Fig. 1 indicates fins on the air side passages, which are often louvered (not shown in the illustration) to enhance heat transfer, since air side cooling typically presents the highest resistance to heat transfer.

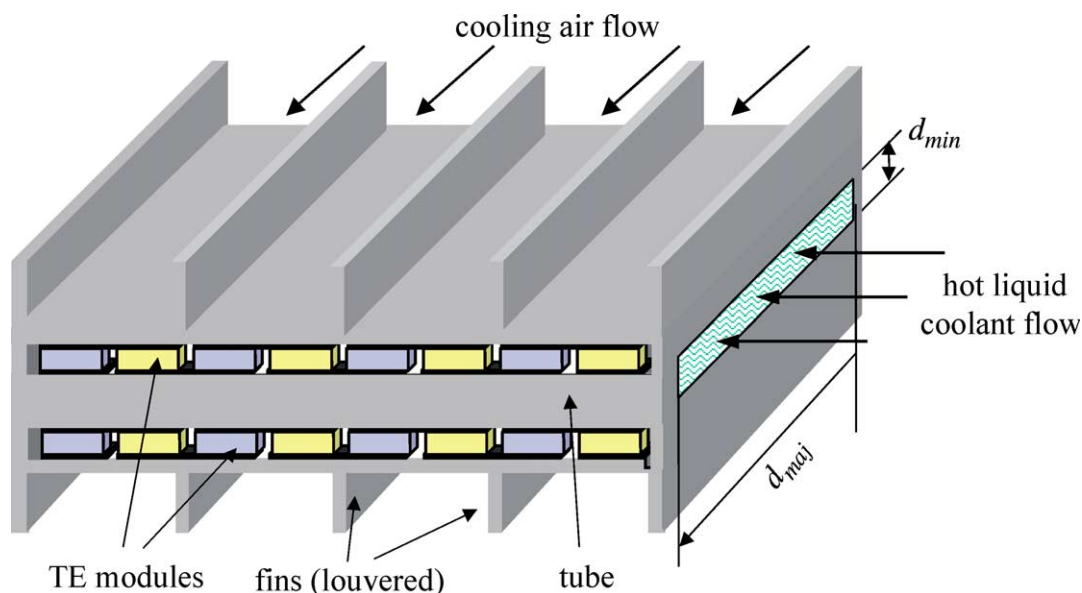


Fig. 1. Schematic showing layout of sub-section of thermoelectric heat exchanger.

The numerical model incorporates the systems level power requirements associated with both pumping the heat source (liquid) and blowing the cooling air through the exchanger. The numerical model is validated in two parts. The heat exchanger model is validated against measured performance of advanced cross flow heat exchangers without thermoelectrics, and the part of the model with integrated thermoelectric modules is validated against simple experiments using thermoelectrics between counterflow hot water and cooling air flow channels. The full model is used in a systems level optimization to determine the optimal performance/design of thermoelectric power generators for waste heat recovery from hot water/glycol mixture streams. Optimization of a thermoelectric power generation module has been previously presented [13], but these optimization studies did not address system accessories and constraints associated with the external heat transfer. The previous studies indicated, for a given design, longer TE couples tend to produce higher η_{TE} but at the expense of lower ε and, in general, lower η_{th} . Other studies have incorporated power penalties associated with the hot fluid flow pressure drops [14,15], and these studies identified some of the trade offs between TE couple geometry and efficient heat exchange. This new study focuses on simultaneously optimizing both the heat exchanger geometry as well as the TE geometry for optimal net waste heat recovery performance by including the penalties associated with both the hot and cooling flow pressure drops. This study also provides a basis for further analysis as new TE materials and segmented modules become available.

2. Model description

The basic configuration for the optimization study follows the general design suggested by the heat exchanger subsection illustrated in Fig. 1. The TE modules are located along the perimeter on the major axis of the hot flow passages as in Fig. 1. The TE modules are electrically isolated by thin passivating oxide layers on both the outer surface of the metal tubes, which hold the hot fluid, and the inner surface of the outer metal wall, which supports the fins for air side cooling. Integration of TEs in the heat exchanger design must not cause a significant drop in ε , and this requires that the length of the TE legs remain relatively small. By fixing this basic configuration and varying the heat exchanger and TE geometrical parameters as well as the heating and cooling flow rates, significant insight is gained into the trade offs and principles for optimizing TE waste heat recovery on a systems level.

A numerical model has been developed for a single tube with hot fluid flow, surrounding TE modules and external cooling air flow over extended heat transfer surfaces (i.e. this case, louvered fins). The model domain includes half the width of the external cross flow passages on both sides of the tube. Thus, under the assumption that all hot fluid flow tubes are performing equally, the mid-plane boundary in the cross flow passage between adjacent tubes acts as an adiabatic surface, and a single tube model can capture the performance of the entire thermoelectric heat exchanger. For optimization studies, the dimensions of the tubes and the extended surface features in the cross flow cooling passages are free to vary with the number of tubes in a fixed volume to determine optimal net power densities. The model is set up with the option to exclude the thermoelectric modules surrounding the heat exchanger tube in order to validate the cross flow heat transfer correlations against experiments of similarly designed heat exchangers. For this study, the

heat exchanger design is constrained to a single row of tubes, rather than multiple rows of inline or staggered tubes.

2.1. Heat exchanger modeling

In order to facilitate parametric design optimization, the heat exchanger model implements empirical correlations for the hot side and cold side convective heat transfers. For the hot fluid flow through the inner tube, the Nusselt number, $Nu_f = \frac{h_f d_{\text{tube}}}{\lambda_f}$, uses correlations for fully developed pipe flow, since the ratio of l_{tube} to hydraulic diameter d_{tube} typically ranges from 40 to 100. For the laminar flow regime, Nu_f , assuming constant wall temperature, varies from 2.9 to 7.5 with variations in the aspect ratio of the tubes ($d_{\text{maj}}/d_{\text{min}}$) [16]. For transition and turbulent flow conditions, Gnielinski's correlation for Nusselt number is used, where the property values are evaluated at the local fluid temperature T_f [16].

$$Nu_f = \frac{(f_f/2)(Re_f - 1000)Pr_f}{1 + 2.7(f_f/2)^{1/2}(Pr_f^{2/3} - 1)} \quad (3)$$

The Fanning friction factor f_f for the tube flow is calculated for all flow regimes using the following formula developed by Bhatti and Shah [17]

$$f_f = A + \frac{B}{Re_f^{1/m}} \quad (4)$$

where for laminar flow ($Re_f < 2100$), $A = 0$, $B = 16.0$ and $m = 1.0$, for transition flow ($2100 < Re_f \leq 4000$), $A = 0.0054$, $B = 2.3 \times 10^{-8}$ and $m = -0.6667$, and for turbulent flow ($Re_f > 4000$), $A = 0.00128$, $B = 0.1143$ and $m = 3.215$. Using this Fanning friction factor, the fluid side pressure are drop and associated pumping work are calculated.

For the external cooling air flow, the heat transfer coefficient over the extended surface uses a previously developed correlation [18]

$$h_a = \frac{j\dot{m}_a C_{p,a}}{A_0 Pr_a^{2/3}} \quad (5)$$

where the Colburn factor, j , is taken from a generalized correlation for a corrugated louver fin geometry for cross flow heat exchangers [19].

$$j = 1.18 Re_a^{-0.505} \left(\frac{\theta}{90}\right)^{0.26} \left(\frac{d_{\text{maj}}}{p_{\text{louv}}}\right)^{-0.26} \left(\frac{l_{\text{fin}}}{p_{\text{louv}}}\right)^{-0.51} \left(\frac{t_{\text{fin}}}{p_{\text{louv}}}\right)^{-0.097} \left(\frac{p_{\text{tube}}}{p_{\text{louv}}}\right)^{-0.25} \left(\frac{l_{\text{louv}}}{p_{\text{louv}}}\right)^{0.82} \quad (6)$$

where Re_a is calculated with the velocity at A_0 and a length scale of p_{louv} . This correlation was validated from a compilation of many studies for a range of louver geometries and shows good agreement with experiments ($\pm 25\%$ for 98% of the samples compared) over a broad range of flow conditions with Re_a ranging from 100 to 3000. Although other correlations exist for flow over louvered fins [20–23], the above correlation was chosen for the extent of its validation and its more general nature.

The cooling air flow pressure drop, which determines the required cooling fan power, is calculated by using [24]

$$\Delta P_a = \frac{\dot{m}_a^2}{2A_0^2 \rho_{a,in}} \left[(1 + \sigma^2) \left(\frac{\rho_{a,in}}{\rho_{a,out}} - 1 \right) + \frac{f_a A_{ht}}{A_0} \frac{\rho_{a,in}}{\rho_{a,mean}} \right] \quad (7)$$

where f_a is based on Re_a [25]

$$f_a = 0.805 Re_a^{-0.514} \left(\frac{p_{fin}}{p_{louv}} \right)^{-0.72} \left(\frac{l_{fin}}{p_{louv}} \right)^{-1.22} \left(\frac{l_{louv}}{p_{louv}} \right)^{1.97} \quad (8)$$

The friction factor correlation is valid for $Re_a = 100 - 700$ and ratios of louver fin surface area to outer tube surface area ranging from 7 to 12. Other friction factor correlations for different louvered fin geometries exist [23], but the selected correlation provides consistency with the heat transfer correlation. A comprehensive analysis comparing different louver fin designs has not been completed for this study.

2.2. Thermoelectric modeling

As stated in the introduction, thermoelectric modules of Bi_2Te_3 are well suited for applications for low temperature waste heat recovery. The TE properties for both p-type and n-type Bi_2Te_3 semiconductors are calculated by using information provided by Melcor, Inc. [26]. A simple energy balance around the TE modules yields the following equations for the hot side heat flux into the TEs, the cold side heat flux out of the TEs and the power generated per unit surface area of the hot fluid tube:

$$\dot{q}_{sh} = \left(K_{TE}(T_{sh} - T_{sc}) + \alpha T_{sh} I - \frac{1}{2} I^2 R_{TE} - I^2 R_c \right) * n_{TE} \quad (9)$$

$$\dot{q}_{sc} = \left(K_{TE}(T_{sh} - T_{sc}) + \alpha T_{sc} I + \frac{1}{2} I^2 R_{TE} + I^2 R_c \right) * n_{TE} \quad (10)$$

$$\dot{w}_{TE} = (\alpha(T_{sh} - T_{sc})I - I^2(R_{TE} + 2R_c)) * n_{TE} \quad (11)$$

The material properties for the thermoelectrics in Eqs. (9)–(11) vary along the length of the hot fluid tube with changes in temperature. The electrical contact resistance R_c between the p and n couples was taken into account as in previous references [2,27].

Thermal contact resistance arises between the TE couple interconnects and the oxide layers on the heat exchanger material. It is taken into account by simulating a partial air gap, which increases the resistance to heat transfer and causes a small drop in T_{sh} between the two adjoining surfaces. These air gaps represent the surface irregularities in the layers, which increase the resistance to heat transfer and thereby reduce the temperature difference across the TE couples.

The current flow through the thermoelectrics for a given side wall of a heat exchanger tube is determined by the number of couples aligned in series.

$$I_{TE} = \frac{\sum_{i=1}^n (\alpha(T_{sh} - T_{sc})n_{TE} * d_{maj}\Delta x)_i}{R_{load} + \sum_{i=1}^n ((R_{TE} + 2R_c)n_{TE} * d_{maj}\Delta x)_i} \quad (12)$$

where $n = l_{tube}/\Delta x$. The numerator in Eq. (12) is the sum of the voltages generated in each i th segment of the axial discretization, and the summation in the denominator represents the internal

resistance due to the couples and contact resistances in each segment. Eq. (12) applies when the thermoelectric modules are wired in series along each tube but in parallel for separate tubes. The power per tube is simply $I^2 R_{\text{load}}$.

2.3. Numerical approach

The numerical model is implemented in MATLAB. The primary discretization is along the axial direction of the hot fluid flow, which is captured with a first order upwind differencing scheme. The transverse heat transfer out of the hot flow is modeled using the above heat transfer correlations and TE analysis. Thermal conduction, both across and along the walls of the tubes, is incorporated using central differencing discretization for the gradients. For the air side cross flow, the log mean temperature is solved for at each axial location and is used to determine the heat transfer to the cooling air flow.

The cells are set at a constant length Δx , specified as a multiple of the distance between adjacent rows of thermoelectric couples. For the scenarios in this paper, Δx ranges from 1 to 2 cm. In light of the mild temperature gradients across the heat exchanger, this level of discretization is determined to be more than adequate for accurately modeling the variation in heat fluxes and thermoelectric power across the tube length. The discretized energy conservation equations, as discussed in detail in previous references [28,29], lead to equations at all axial distances along the tube flow for T_f , T_{sh} , T_{sc} , T in the inner and outer tube walls and the log mean of T_a . The model solves these non-linear governing equations simultaneously for the steady state temperatures via an iterative Newton–Raphson method using an analytical Jacobian.

Along with the temperatures, the current flow through the thermoelectric couples, I , must be determined. Since the couples for each tube are wired in series, as indicated by Eq. (13), I is constant for all axial positions. Numerically, the global nature of I causes the Jacobian of the governing equations to lose its block tri-diagonal structure, which slows the Newton–Raphson's iterations, although not prohibitively.

3. Experimental validation

3.1. Thermoelectric heat transfer validation experiment

An experiment was set up to validate the heat transfer model through the thermoelectrics as detailed above. A block diagram of the experiment is shown in Fig. 2. A single aluminum tube (40 mm × 8 mm × 0.5 mm), which flowed hot water, was lined on each side with three TE modules (0.4 cm thick) that included thin Al_2O_3 plates around the TE couples. On the cold side of the TE modules, aluminum tubes for the cooling air flows were pressed against the TE ceramic insulating plate (as shown in Fig. 2). Silver based thermal grease (manufactured by Arctic Silver Inc.) was placed between all of the ceramic plate/flow tube interfaces in order to minimize the thermal contact resistance.

Hot water through the center tube was pumped around a short closed loop system that included a reservoir with a temperature controlled immersion heater and a flow meter as indicated in Fig. 2. To ensure even distribution of the water flow through the tube, flow straighteners were used at the

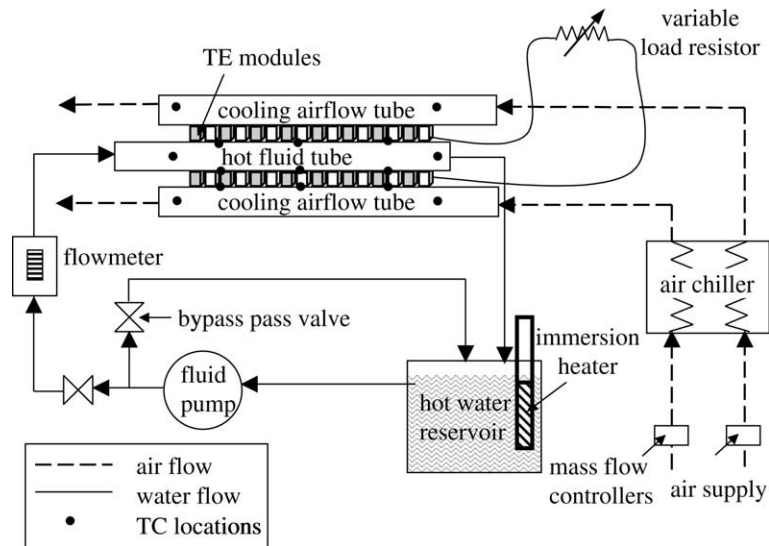


Fig. 2. Schematic of counterflow TE heat exchanger experiments used for TE model validation.

exit to backpressure the water flow and force it to wet the entire tube surface. Electronic mass flow controllers controlled the high air flows through the cooling tubes. The air flows in the counterflow heat exchange configuration provided high cooling and permitted the use of a well established heat transfer correlation in modeling the experiments. This allowed the modeling of this validation experiment to focus on the models for the TE module effective conductivity and contact resistances. Temperature measurements were made using K-type thermocouples at the inlet and outlet of each of the tubes. In addition, thermocouples were placed at the center of each of the ceramic surfaces of the TE modules.

Heat leakage from the outer tube walls forced the experimental model to incorporate heat losses from the minor dimension on the hot fluid flow tube and from the outer walls on the cooling air flow tubes. The heat losses were determined through fits used to match the changes in temperature and power output as a function of load resistance. Although the heat losses were kept small with alumina-silicate fiber insulation around the rig, modeling these losses was necessary to capture the observed $(T_{sh} - T_{sc})$. Computer simulations from the revised model were compared with experimental results for the configuration shown in Fig. 2. A least squares optimization was used to determine the heat transfer coefficients for the external heat losses and to fit the thermal contact resistances between the ceramic layers around the TE couples and the metallic tubes. In addition, the electrical contact resistivity ρ_c was determined by a least squares fit of the experimental data to the model predictions. A value of $5 \times 10^{-12} \Omega \text{ m}^2$ was found to give good agreement with the contact resistances that have been measured and reported in the literature [30,31]. Over 35 experimental cases were performed for a range of hot fluid and cooling air flows and for a wide range of TE power conditions, such that the results could be used to evaluate the TE heat transfer model.

The thermal contact resistances were evaluated in terms of an equivalent air gap thickness between the ceramic plates of the TE module and the flow tubes on the hot and cold sides of the

TE. Thicknesses for the equivalent air gaps were calculated to be only a few hundredths of a millimeter, and the effective thermal contact resistances for the experimental conditions were found to be $\sim 1400 \text{ W/m}^2 \text{ K}$, which also corresponds well with values reported in the literature [32].

Results from the validation experiments are summarized in Figs. 3 and 4. Fig. 3 plots current versus power where the curves were generated by varying the external load resistance, R_{load} , at

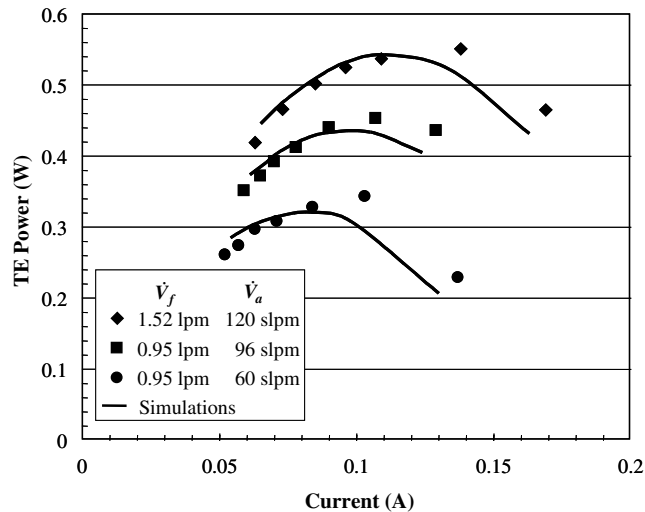


Fig. 3. Experimental data and model results for TE power versus current for three different sets of conditions. Curve was created by taking measurements at various load resistances.

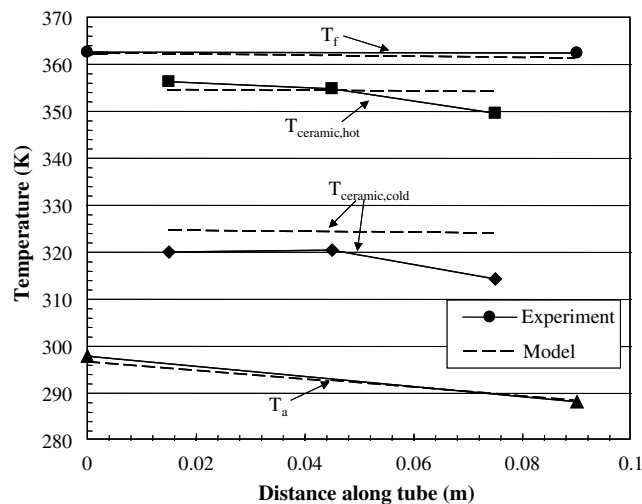


Fig. 4. Temperature along tube for the hot fluid, cold air and on the hot and cold ceramic surfaces of the thermoelectrics ($\dot{V}_f = 1.52 \text{ lpm}$, $\dot{V}_a = 120 \text{ slpm}$).

different fluid and air flows. Previous studies have reported that the maximum power of a TE module is achieved when R_{load} equals the effective internal resistance of the module [1,2,27]. The calculated total internal resistance for the three curves in Fig. 3 are $33.6 \pm 0.4 \, \Omega$ and the peak of the simulated power curves occurs where R_{load} equals the internal resistance.

Fig. 4 compares the measured temperatures with those predicted by computer simulation. Agreement is within $\pm 2 \, \text{K}$ except for the cold side temperature of the TE ceramic. The experimental cold side temperature is lower than the simulated temperatures most likely because the experimental measurement was taken at the interface of the TE ceramic with the surrounding metal tube and, thus, took an average of the temperatures on the inside of the cooling air tube and the outside of the TE module ceramic plate.

A sensitivity study on the computational model results was implemented to explore sources of variation between the experimental and model results. The dimensionless sensitivity coefficients are highest for the initial cooling air and hot fluid temperatures. A 1% change in initial fluid temperature can cause as much as a 15% change in power output for some conditions. This large sensitivity of power to fluid temperature made it critical to use actual experimentally measured conditions when validating the model and further suggests why the simulation curves for power in Fig. 3 deviate from the experimental data for some cases.

The relative magnitudes of the resistances to heat transfer between the hot fluid and the cooling air in the experimental configuration can be inferred from the temperature plots in Fig. 4. Even with the high air velocities in the experiments, the cold air side heat transfer is not optimal, and 40% of the overall temperature drop occurs between the thermoelectric module and the cooling fluid, as suggested in Fig. 4. Nonetheless, for the experiments, approximately 40% of the total temperature drop between T_f and T_a does occur across the TE module, which indicates that these experiments provided a useful configuration for validating the heat transfer model for the TEs. An optimal heat exchanger for waste heat recovery would maximize this temperature difference across the TE couples by having minimal heat transfer resistance and, thus, temperature drop at both the hot and cold side fluid–wall interfaces.

3.2. Cross flow heat transfer validation

The cross flow correlations for the air side heat transfer were implemented and validated for heat exchangers without thermoelectrics in a similar manner as previously reported [19]. Typical cross flow heat exchanger specifications were used as a baseline, both to validate the model and to ascertain what were reasonable limitations on dimensions for a design optimization. For this study, the heat exchanger dimensions were similar to those of a stock cross flow heat radiator (manufactured by Harrison Thermal Systems for a GM Chevrolet Suburban).

The cross flow heat exchanger model was validated against actual radiator performance data without thermoelectric modules, and some of the results are shown in Fig. 5a and b. The model predicts the axial drop in coolant temperature, ΔT_f , to within 4% for the entire range of \dot{V}_a and \dot{V}_f as indicated in Fig. 5a. The model also captures the experimental variation of the pressure drops with flow rates, both ΔP_a with \dot{V}_a and ΔP_f with \dot{V}_f . The variation of ΔP_a with \dot{V}_a is plotted in Fig. 5b, and the results indicate that the model under predicts ΔP_a by no more than 25% at the highest air flow rates. ΔP_f as a function of \dot{V}_f is captured to within 5% over the entire range of flow rates and is, therefore, not shown in Fig. 5. The model validation with the radiator data provides

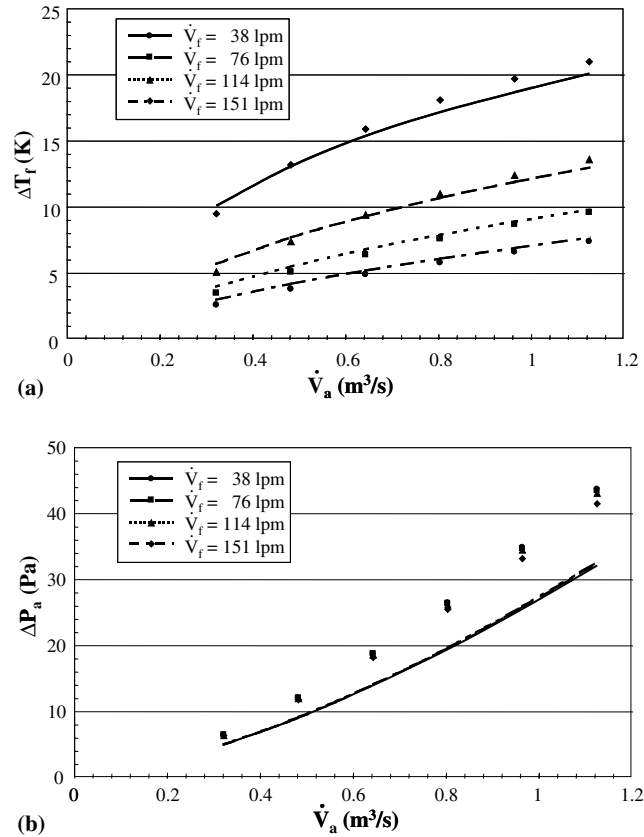


Fig. 5. Results from radiator validation study based on data from Harrison thermal systems. Model results indicated by lines and experimental data indicated by points. (a) Coolant temperature drop across radiator as a function of air flow over radiator tubes for a range of coolant fluid flows. (b) Air side pressure drop in cross flow as a function of air flows for a range of coolant fluid flows.

confidence that the hot and cold flow heat transfers and pressure drops are captured well enough that the power, \dot{W}_{TE} , produced by the TE couples placed between the hot and cold side walls can be calculated to a desirable degree of accuracy. With the validated heat transfer correlations and the TE model parameters, the model was established for optimizing a cross flow heat exchanger for TE waste heat recovery.

4. Optimization study

With the cross flow heat exchanger model integrated with the models for the TE couples, an algorithm was implemented to optimize the cross flow heat exchanger configurations for waste heat recovery. The objective function for the optimization is the net power (\dot{W}_{net}) divided by the heat exchanger cost. \dot{W}_{net} is calculated as the total TE power output from the heat exchanger minus the expected power to operate an electric fan for the cooling air flow and an electric pump

for the hot fluid (a water/glycol mixture). The cost includes the thermoelectric and aluminum cost of the heat exchanger. The aluminum cost is derived from cost rates for commercially available radiators, and the cost of the thermoelectrics is derived from the bulk cost rates for commercially available TE materials. The TE cost is divided into manufacturing cost per couple, material cost per volume of TE material and assembly cost per TE module. These costs are best estimates, and the optimal solution will be influenced to some degree by changes in the cost functions. Previous studies looked at optimizing costs for integrated thermoelectric heat exchangers based on varying fuel costs [13,33], but unlike the current study, the earlier optimizations focused on the effects of TE area and leg length without looking at the total system cost and net energy output.

The objective function for the current optimization, $F(\vec{X})$, where \vec{X} is the vector of optimization variables, is shown here:

$$F(\vec{X}) = \frac{\dot{W}_{\text{net}}}{(\$_{\text{TE}} + \$_{\text{HE}})} = \frac{\dot{W}_{\text{TE}} - \dot{W}_{\text{pump}} - \dot{W}_{\text{fan}}}{(\$_{\text{TE}} + \$_{\text{HE}})} \quad (13)$$

$$\vec{X} = [d_{\text{maj}}, d_{\text{min}}, l_{\text{TE}}, w_{\text{TE}}, p_{\text{fin}}, p_{\text{tube}}, \dot{V}_{\text{a}}, \dot{V}_{\text{f}}]^T \quad (14)$$

In order to ensure that reasonable solutions are found, bounds are placed upon the variables in \vec{X} . The upper and lower bounds for all variables in \vec{X} are set as discussed in detail elsewhere [29] and, in general, follow standard cross flow heat exchanger geometries and expected manufacturing limitations. An additional constraint is set to ensure $d_{\text{maj}}/d_{\text{min}} > 5.0$ in order to avoid having substantial amounts of heat loss through the minor dimension of the tube where no TE couples are located. A final constraint implemented to ensure that the optimization scheme does not converge to a low cost heat exchanger with minimal power output by forcing the heat exchanger to have a $\dot{W}_{\text{net}} \geq 1.0$ kW.

An optimized solution for the cross flow heat exchanger design with a frontal area of $1 \text{ m} \times 1 \text{ m}$ is listed in Table 1. The net power output of the optimal solution is the minimum of 1 kW, with a current of 0.71 A per tube and a voltage of 70.8 V for each tube. Wiring each tube in parallel keeps the voltage < 100 V. Cost increases outweighed increases in \dot{W}_{net} above 1 kW, thus providing lower power/cost ratios.

To assess the importance of different parameters for optimizing the heat exchanger, a parametric study was performed on the design using the optimal solution as the baseline case. The

Table 1

Optimal design for remote heat exchanger based on power/cost ratio (kW/\$10,000) objective function and constant load impedance of 50 Ω

| Design variables | | Performance outputs | |
|----------------------|------------------------|--|------------------|
| d_{maj} | 2.23 cm | $\dot{W}_{\text{net}}/(\$_{\text{HE}} + \$_{\text{TE}})$ | 1.09 kW/\$10,000 |
| d_{min} | 0.45 cm | \dot{W}_{net} | 1.00 kW |
| p_{fin} | 0.13 cm | \dot{W}_{TE} | 1.34 kW |
| p_{tube} | 3.74 cm | \dot{Q}_{TE} | 63.08 kW |
| l_{TE} | 0.17 cm | η_{TE} | 2.12% |
| w_{TE} | 0.20 cm | I_{TE} | 0.71 A |
| \dot{V}_{a} | 2.12 m ³ /s | R_{Internal} | 27.4 Ω |
| \dot{V}_{f} | 294.1 lpm | | |

effects of the variation of TE leg length on net power output and the power/cost ratio function F are shown in Fig. 6a. The peak at the optimal design point occurs because of a trade off between η_{TE} and ε . Although higher η_{TE} is achieved with longer leg lengths [13], the longer leg lengths create more restriction to the air flow between the heat exchanger tubes and, thus, greatly reduce ε . Previous studies of single tubes have shown that when the electrical contact resistances are negligibly small, the power output increases with TE leg lengths being as short as manufacturing will allow. However, these power gains come at the expense of reduced η_{TE} . On the other hand, as shorter leg lengths reduce the electrical and thermal resistances, the contact resistances begin to become significant and negatively impact both η_{TE} and ε [10,13,32]. The results in Fig. 6a suggest that for $l_{TE} < 0.15$ cm, the contact resistances begin to decrease the net power.

With λ_f being nearly 30 times higher than λ_a , h_a is $\sim 3\%$ of h_f . Thus, increases in heat transfer surface area on the cold side are needed to avoid the cold side surface to air heat transfer becoming the dominant resistance to heat flow. The need for increased air side surface area is reflected in the values for optimal d_{maj} and n_{tube} shown in Fig. 6b and c. Increases in both of these parameters greatly enhance the cold side heat transfer, but maxima arise in \dot{W}_{net} because ΔP_a and the associated \dot{W}_{fan} increase with d_{maj} and n_{tube} due to increased wall friction and decreased air flow area, respectively. A similar maximum in \dot{W}_{net} is found for p_{fin} as it decreases because the increased number of fins improves the air side heat transfer but at the expense of reduced flow area and increased friction for the air flow. However, for the optimal solution in Table 1, p_{fin} approaches the manufacturing constraints (~ 0.1 cm), which indicates the significance of increasing the heat transfer area on the air side.

Fig. 6b shows how the power/cost ratio and \dot{W}_{net} vary differently with d_{maj} . The highest power/cost ratios occur only when $\dot{W}_{net} < 1$ kW, and thus, the optimal point shown in Table 1 is not at the highest possible value of F due to the power constraint of the objective function. As d_{maj} increases, the cost of the exchanger increases faster than \dot{W}_{net} because the addition of more TE couples (which is the major cost factor) does not produce proportionally as much increase in power.

The tube spacing, p_{tube} , also has a major impact on the TE cost. Therefore, the curves for power/cost ratio and \dot{W}_{net} versus p_{tube} , shown in Fig. 6c, do not follow the same trends. Again, higher than optimal power/cost ratios can be achieved, but these values are only found when the net power output is below the minimum \dot{W}_{net} constraint. The trade offs between increased ΔP_a with the associated increase in \dot{W}_{fan} and increased \dot{W}_{TE} by decreasing p_{tube} cause the observed peak in \dot{W}_{net} with p_{tube} in Fig. 6c. If p_{tube} is too high, the reduced number of thermoelectrics results in inadequate electric power to outweigh the losses for driving the flows.

For the optimization studies above, R_{load} was kept constant at 50 Ω per tube. As can be seen from Table 1, the TE internal resistance per bank of modules on each tube side is $\sim 27 \Omega$, which is approximately equal to $R_{load}/2$. As discussed earlier, the theoretical maximum power output of a thermoelectric generator system occurs when the TE internal resistance equals R_{load} . The difference in internal resistance and R_{load} at the optimal design point arises because of the penalties included for costs and accessory power demand.

Fig. 7a shows how \dot{W}_{TE} , \dot{W}_{pump} , and \dot{W}_{net} vary with \dot{V}_f for the optimal design geometry presented in Table 1. As \dot{V}_f increases, \dot{W}_{TE} increases, but above 300 lpm, the increases in \dot{W}_{TE} are outweighed by the increases in \dot{W}_{pump} , and thus, there is a peak in \dot{W}_{net} at $\dot{V}_f = 295$ lpm. Similarly, Fig. 7b shows the peak in \dot{W}_{net} with increases in \dot{V}_a . Increases in \dot{V}_a more significantly impact \dot{W}_{TE}

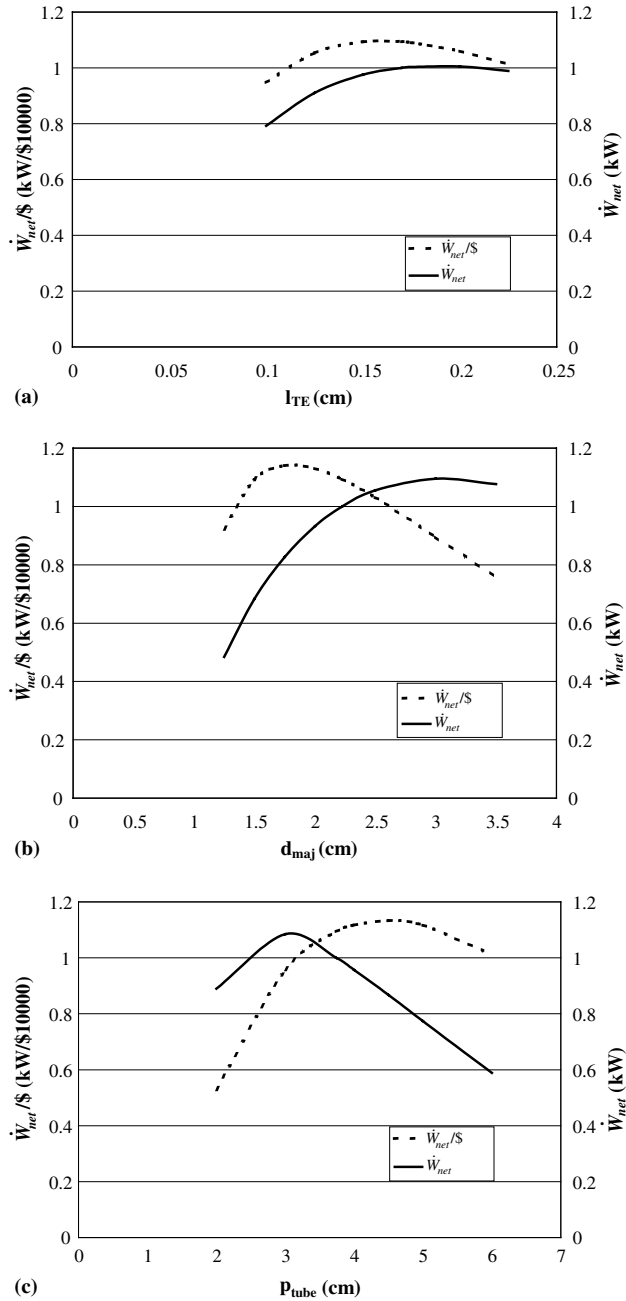


Fig. 6. Changes in power/cost ratio and net power output with variation in single parameter from optimal point: (a) l_{TE} , (b) d_{maj} and (c) n_{tube} .

than increases in \dot{V}_f . However, the dramatic increase in \dot{W}_{TE} with \dot{V}_a comes with a rapid increase in \dot{W}_{fan} , and \dot{W}_{net} has a sharp peak at the optimal point where $\dot{V}_a = 2.12 \text{ m}^3/\text{s}$. For all the TE heat

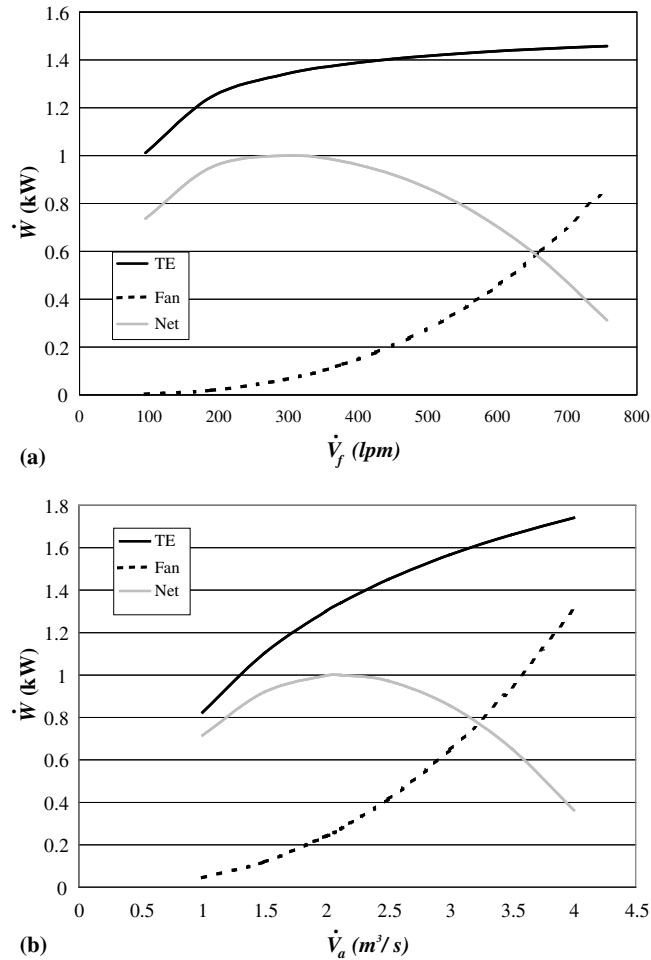


Fig. 7. Changes in TE and net power output with variation in flow rate for optimized remote heat exchanger: (a) \dot{V}_f with associated pump power, (b) varying \dot{V}_a with associated fan power.

exchanger designs, increases in \dot{V}_a or \dot{V}_f increase the fan or pump power, respectively and, at some point, outweigh the gains in TE power generated, and thus, net power reaches a maximum at intermediate flows.

5. Conclusion

A numerical model has been created for an integrated thermoelectric heat exchanger in a cross flow configuration. The features of the model have been validated with cross flow heat exchanger data and with simple experiments integrating hot fluid and cooling air flows with Bi_2Te_3 TE modules. The results from the validation studies confirm that the effectiveness of the system is extremely sensitive to the operating temperature range of the thermoelectric device. Using the

validated model, a systems level optimization study was conducted to show the potential of using cross flow heat exchangers with hot side fluid temperatures characteristic of coolant flows for IC engines for TE based waste heat recovery.

The results show that a net power output of 1 kW can be achieved for a modestly sized heat exchanger core such that the net power density based on heat exchanger volume is $\sim 45 \text{ kW/m}^3$. Optimization for a power/cost ratio objective function with a minimum net power requirement of 1 kW indicated that the power per cost can reach as high as 1.1 kW/\$10,000. Parametric studies using the optimal solution as a baseline show the importance of different design variables for waste heat recovery and further elucidate the important design tradeoffs between minimizing the air side ΔP and optimal TE performance. Further work is needed to assess the manufacturing process for integrating TE material into heat exchanger design in a more cost effective manner to reduce the current costs of TE waste heat recovery.

Acknowledgements

The authors would like to acknowledge Mr. Lindsay Litzel at Harrison Thermal Systems Division of Delphi Automotive Systems for valuable insight into critical aspects of heat exchanger design specifications. The authors would also like to thank Prof. David Holloway for helpful discussions on this project.

References

- [1] Angrist SW. Direct energy conversion. 4th ed. Boston: Allyn and Bacon, Inc; 1982.
- [2] Rowe DM, editor. CRC handbook of thermoelectrics. Boca Raton, FL: CRC Press LLC; 1995.
- [3] Mahan GD, Sales B, Sharp J. Thermoelectric materials: new approaches to an old problem. *Phys Today* 1997;42–7.
- [4] DiSalvo FJ. Thermoelectric cooling and power generation. *Science* 1999;285(5428):703–6.
- [5] Chen G et al. Recent developments in thermoelectric materials. *Int Mater Rev* 2003;48(1):45–66.
- [6] Fleurial JP et al. New materials and devices for thermoelectric applications. In: *Intersociety Energy Conversion Engineering Conference*. Honolulu, HI: IEEE; 1997.
- [7] Kang YS et al. Development and evaluation of 3-stage segmented thermoelectric elements. In: *17th International Conference on Thermoelectrics*. Nagoya, Japan: IEEE; 1998.
- [8] Venkatasubramanian R et al. Thin-film thermoelectric devices with high room-temperature figures of merit. *Nature* 2001;413:597–602.
- [9] Ghamaty S, Elsner N. Development of quantum well thermoelectric device. In: *18th International Conference on Thermoelectrics*. Baltimore, MD: IEEE; 1999.
- [10] Nolas GS, Sharp J, Goldsmid HJ. *Thermoelectrics—basic principles and new materials developments*. Berlin, Heidelberg: Springer Verlag; 2001.
- [11] Bass JC, Elsner NB, Leavitt FA. Performance of the 1 kW thermoelectric generator for diesel engines. In: *American Institute of Physics*, 1995, p. 295–98.
- [12] Nagao K et al. Design of thermoelectric generation system utilizing the exhaust gas of internal combustion power plant. In: *17th International Conference on Thermoelectrics*. Nagoya, Japan: IEEE; 1998.
- [13] Rowe DM, Min G. Design theory of thermoelectric modules for electrical power generation. *IEE Proc: Sci, Meas Technol* 1996;143(6):351–6.
- [14] Matsuura K et al. Design optimization for a large scale, low temperature thermoelectric generator. In: *11th International Conference on Thermoelectrics*. Arlington, TX: IEEE; 1992.

- [15] Esarte J, Min G, Rowe DM. Modelling heat exchangers for thermoelectric generators. *J Power Sources* 2001;93:72–6.
- [16] Ebadian MA, Dong ZF. Forced convection internal flow in ducts. In: Rohsenow WM, Hartnett JP, Cho YI, editors. *Handbook of heat transfer*. New York: McGraw-Hill; 1998 [chapter 5].
- [17] Bhatti MS, Shah RK. Turbulent and transition flow convective heat transfer in ducts. In: Kakac S, Shah RK, Aung W, editors. *Handbook of single-phase convective heat transfer*. New York, NY: John Wiley & Sons; 1987.
- [18] Charyulu DG, Singh G, Sharma JK. Performance evaluation of a radiator in a Diesel engine—a case study. *Appl Therm Eng* 1999;19(6):625–39.
- [19] Chang Y-J, Wang C-C. A generalized heat transfer correlation for louver fin geometry. *Int J Heat Mass Transfer* 1997;40(3):533–44.
- [20] Davenport CJ. Heat transfer and flow friction characteristics of louvered heat exchanger surfaces. In: Taborek J, Hewitt GF, Afgan N, editors. *Heat exchangers theory and practice*. Washington, DC: Hemisphere Publishing Corporation; 1983. p. 397–412.
- [21] Sahnoun A, Webb RL. Prediction of heat transfer and friction for the louver fin geometry. *J Heat Transfer* 1992;114(4):893–900.
- [22] Olsson CO, Sunden B. Heat Transfer and pressure drop characteristics of ten radiator tubes. *Int J Heat Mass Transfer* 1996;39(15):3211–20.
- [23] Achaichia A, Cowell TA. Heat transfer and pressure drop characteristics of flat tube and louvered plate fin surfaces. *Exp Therm Fluid Sci* 1988;1:147–57.
- [24] Kays WM, London AL. *Compact heat exchangers*. New York: McGraw-Hill; 1984.
- [25] Chang YJ, Wang C-c, Chang WJ. Heat transfer and flow characteristics of automotive brazed aluminum heat exchangers. In: *ASHRAE Transactions: Symposia*. Orlando, FL: ASHRAE; 1994.
- [26] MELCOR. Available from www.melcor.com/formula.htm. 2003.
- [27] Cobble MH. Analysis of a thermoelectric device having contact resistance. In: *11th International Conference on Thermoelectrics*. Arlington, TX: IEEE; 1992.
- [28] Crane DT, Jackson G, Holloway D. Towards optimization of automotive waste heat recovery using thermoelectrics. In: *Thermal systems management and heat exchangers*. Warrendale, PA: Society of Automotive Engineers; 2001. p. 53–65.
- [29] Crane DT. Optimizing thermoelectric waste heat recovery from an automotive cooling system. Ph.D. dissertation, University of Maryland, College Park, 2003.
- [30] Buist RJ, Roman SJ. Development of a burst voltage measurement system for high-resolution contact resistance tests of thermoelectric heterojunctions. In: *18th International Conference on Thermoelectrics*. Baltimore, MD: IEEE; 1999.
- [31] Gorodetskii SM, Drabkin LA, Nel'son IV. Instrument for measuring the contact resistance of thermoelectric materials (exchange of experience). *Ind Lab* 1991;56(7):820–2.
- [32] Min G et al. Determining the electrical and thermal contact resistance of a thermoelectric module. In: *11th International Conference on Thermoelectrics*. Arlington, TX: IEEE; 1992.
- [33] Rowe DM, Min G. Evaluation of thermoelectric modules for power generation. *J Power Sources* 1998;73(2):193–8.